Virtual Compton Scattering and the Generalized Polarizabilities of the Proton at Q^2 up to 4.0 GeV^2

Charles E. Hyde-Wright, Co-Spokesperson[†], David Hayes, P.E. Ulmer, L.B. Weinstein

Old Dominion University, Norfolk VA

Géraud Laveissière, Co-spokesperson, Helene Fonvieille, Pierre Bertin, Alex Camsonne, Gueorgui Smirnov

Université Blaise Pascal/IN2P3, Clermont-Ferrand, France

Luminita A. Todor

Carnegie Mellon University, Pittsburgh, PA

Julie Roche

The College of William and Mary, Williamsburg, VA

Alan Nathan

University of Illinois, Urbana, IL

Alexandre Deur

University of Virginia, Charlottesville, VA

the Hall A Collaboration

submitted December 2, 2002 to the Jefferson Lab Program Advisory Committee

We propose to measure the Virtual Compton Scattering (VCS) reaction: $ep \to ep\gamma$ at and above π-production threshold at $Q^2 = 0.65$, 1.35, 3.0, and 4.0 GeV^2. We will use the Dispersion Relation formalism of B. Pasquini *et al.*to extract the Generalized electric and magnetic polarizabilities $\alpha(Q^2)$ and $\beta(Q^2)$. We will identify the VCS process by coincidence detection of the scattered electron and recoil proton in the Hall A HRS pair. We request a total of 8 days of beam. Our request includes 94 hours of polarized beam to measure the beam helicity asymmetry above pion threshold. This provides a test of the Dispersion Relation formalism, independent of the values of the polarizabilities.

†Contact person: chyde@odu.edu

I. INTRODUCTION

The internal charges and currents of a composite system polarize in response to external electromagnetic fields. In a weak external field, the linear response is quantified by the polarizability. In a quantum system, the polarizability is a dispersion integral over the excitation spectrum. Thus the polarizability is a simple observable which summarizes information about the full structure of the target at all energies.

The Q^2 dependence of the polarizabilities (see below) measures the spatial distribution of the response of the proton to an external electro-magnetic field. Naïvely, the spin degree of freedom of quarks will give rise to a paramagnetic response, whereas the motion of charges (quarks or pions) will generate a diamagnetic response. The polarizabilities of the proton have been calculated in Chiral Perturbation Theory for $Q^2 \leq m_\pi^2$ [15]. These calculations show strong contributions from both pion and quark degrees of freedom (the latter are parameterized by resonance terms).

In a non-relativistic system, the electric polarizability scales as α_{QED} times the volume of the system times the ratio of the linear size of the system divided by the compton wavelength of the constituents. Thus the small value of the proton polarizability relative to the proton charge radius is direct evidence for the relativistic character of the structure of the proton.

The high Q^2 behavior of the polarizabilities will complement the new high precision measurements of G_E and G_M in quantifying the nature of charge and magnetism inside the proton. The dispersion relation calculations discussed below provide insight into the range of excitations and the intermediate channels responsible for both the electric and magnetic polarizabilities, as a function of Q^2.

A. Polarizabilities and Real Compton Scattering

The compton scattering amplitude on the proton ($\gamma p \to \gamma p$) is an integral over all possible (real or virtual) intermediate states. To $\mathcal{O}(\omega^2)$, the low energy spin independent amplitude is defined by just the proton mass, charge, magnetic moment, and the electric and magnetic polarizabilities α_E and β_M, where ω is the photon energy in the lab frame [1]. To $\mathcal{O}(\omega^3)$, the [nucleon] spin-dependent amplitude is defined by the same static constants, and four spin dependent polarizabilities γ_{E1}, γ_{M1}, γ_{E2}, and γ_{M2} [1]. The polarizabilities α_E and β_M

enter the unpolarized real compton scattering cross section to order ω^2, from the interference between the polarizability term and the ω-independent (Thomson scattering) term.

B. Polarizabilities and Virtual Compton Scattering

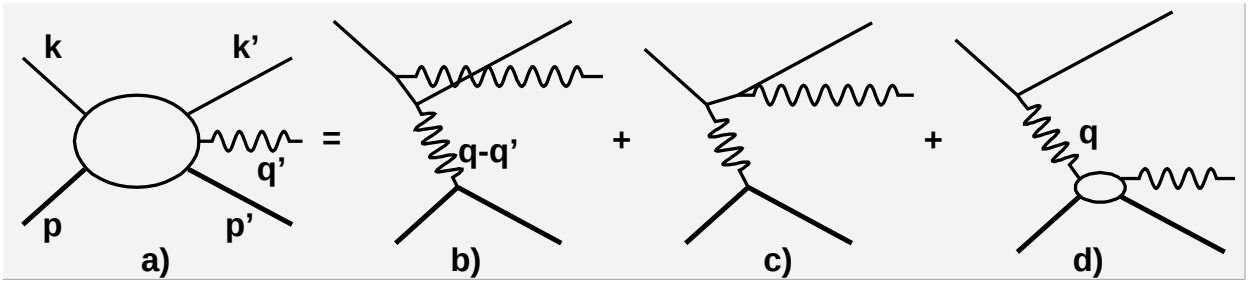

FIG. 1: Lowest order in α_{QED} feynman diagrams for the reaction $ep \to ep\gamma$. a) Kinematic definitions; b) & c) Bethe-Heitler process, pre- & post-radiation, respectively. This is the radiative tail of elastic electron scattering, including in particular the wide angle emission of the photon; d) Virtual Compton Scattering (VCS) amplitude. Some convenient invariants include $Q^2 = -q^2 = -(k-k')^2 > 0$; $s = (q+p)^2$, $t = (q-q')^2$, $u = (p-q')^2$ and $\nu = (s-u)/(4M_p)$.

The virtual compton scattering (VCS) process $ep \to ep\gamma$ is the superposition of the Bethe-Heitler (BH) and Compton processes illustrated in Fig. 1. The figure also defines our kinematic conventions. It is convenient to make the [gauge invariant] separation of the compton process into the nucleon Born (B) terms and non-Born (NB) terms, as illustrated in Fig. 2. The non-Born terms contain all of the dependence of the VCS amplitude on the continuum spectrum of the nucleon.

P. Guichon, G. Liu, and A. Thomas [3] derived a low energy theorem for the VCS amplitude as a function of q', the final photon energy in the γp Center-of-Mass (CM) system. The Bethe-Heitler and Born terms of the VCS amplitude have the expansion:

$$T^{BH+B} \;=\; \frac{a_{-1}}{q'} + a_0 + a_1\, q' + \mathcal{O}(q'^2) \tag{1}$$

The Non-Born amplitude is a regular function of q'_μ. Consequently, the low energy expansion of the Non-Born amplitude starts with a term linear in q':

$$T^{NB} \;=\; b_1\, q' + \mathcal{O}(q'^2) \tag{2}$$

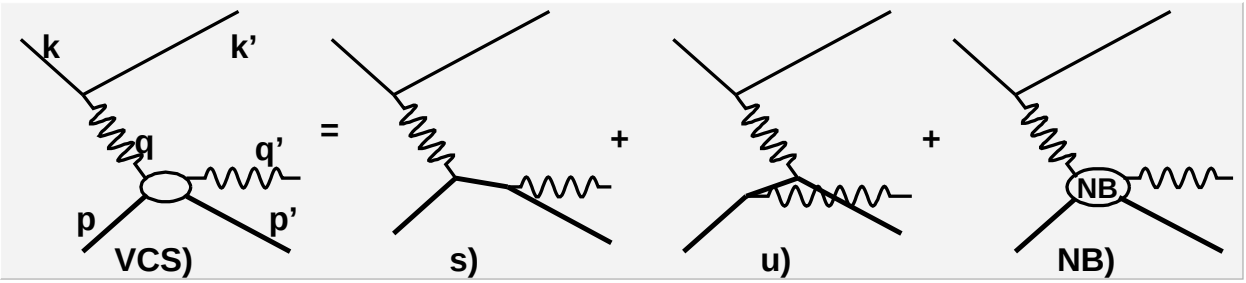

FIG. 2: Separation of the virtual compton amplitude: VCS) into s- and u- channel Born terms and non-Born: NB) terms. The s- and u-channel Born terms depend only on the on shell Dirac and Pauli form factors F_{1p} and F_{2p}. The non-Born terms include the sum over all possible s- and u-channel resonances, or equivalently the sum over all t-channel resonances.

The leading Non-Born term b_1 is determined by all possible couplings of the initial state virtual photon with a final state electric- or magnetic-dipole photon. These are the generalized polarizabilities (GP) of the proton.

A. Metz and D. Drechsel [4] showed in the context of the Linear σ-model that there are just six independent polarizabilities. This was later shown to be a general result [5]. These six independent generalized polarizabilities $P^{\Lambda' L', \Lambda L} S$, as defined by P. Guichon and M. Vanderhaeghen[6], are labeled by the multipolarities of the incident (ΛL) and final $(\Lambda' L')$ photons, and the spin transfer S to the proton, with $\Lambda = C, E, M$ and $S = 0, 1$. A Siegert relation is used to transform electric to coulomb multipoles. The resulting generalized polarizabilities and their $Q^2 \to 0$ limits are:

$$
\begin{aligned}
P^{(C1,C1)0}(Q^2) &\longrightarrow -\sqrt{\frac{2}{3}}\frac{\alpha_E}{\alpha_{QED}} \\
P^{(M1,M1)0}(Q^2) &\longrightarrow -\sqrt{\frac{8}{3}}\frac{\beta_M}{\alpha_{QED}} \\
P^{(C1,C1)1}(Q^2) &\longrightarrow 0 \\
P^{(M1,M1)1}(Q^2) &\longrightarrow 0 \\
P^{(C1,M2)1}(Q^2) &\longrightarrow -\frac{\sqrt{2}}{3}\frac{\gamma_{M2}}{\alpha_{QED}} \\
P^{(M1,C2)1}(Q^2) &\longrightarrow -\frac{2\sqrt{2}}{3\sqrt{3}}\frac{\gamma_{E2}}{\alpha_{QED}}
\end{aligned}
\tag{3}
$$

In terms of these polarizabilities, the unpolarized VCS cross section has the low energy

expansion:

$$\frac{d^5\sigma}{dk'd\Omega'd\Omega^{CM}_{\gamma*\gamma}} = \frac{d^5\sigma^{BH+B}}{dk'd\Omega'd\Omega^{CM}_{\gamma*\gamma}} + \frac{(2\pi)^5}{64M}\frac{k'_{\rm lab}}{k_{\rm lab}}\frac{q'}{\sqrt{s}}\Big\{ v_{LL}\left[P_{LL}(\tilde{Q}^2) - P_{TT}(\tilde{Q}^2)/\epsilon\right] + v_{LT}P_{LT}(\tilde{Q}^2) + \mathcal{O}(q')\Big\} \quad (4)$$

$$P_{LL}(\tilde{Q}^2) = -2\sqrt{6}M_P G_E(\tilde{Q}^2)P^{(C1,C1)0}(\tilde{Q}^2) \quad (5)$$

$$P_{TT}(\tilde{Q}^2) = 3G_M(\tilde{Q}^2)\vec{q}^{\,2}_{CM}\left[\sqrt{2}P^{(C1,M2)1}(\tilde{Q}^2) - P^{(M1,M1)1}(\tilde{Q}^2)/\tilde{q}^0\right] \quad (6)$$

$$P_{LT}(\tilde{Q}^2) = \sqrt{\frac{3}{2}}\frac{M_p|\vec{q}|}{\sqrt{\tilde{Q}^2}}G_E(\tilde{Q}^2)P^{(M1,M1)0}(\tilde{Q}^2) + \frac{3}{2}\sqrt{\tilde{Q}^2}\frac{|\vec{q}|}{\tilde{q}^0}G_M(\tilde{Q}^2)P^{(C1,C1)1}(\tilde{Q}^2) \quad (7)$$

The kinematic factors v_{LL} and v_{LT} are defined in [6]. The "tilde" variables are defined in the $q'_{CM} \to 0$ limit: $\tilde{q}^0 = M_p - \tilde{E}_p = M_p - \sqrt{M_p^2 + \vec{q}^{\,2}}$ (CM frame), $\tilde{Q}^2 = -2M_p\tilde{q}^0$.

Three of the spin polarizabilities enter into Eq. 4. The interference of the compton amplitude with the spin-dependent Bethe-Heitler and Born processes produces this sensitivity to the spin polarizabilities in the unpolarized VCS cross section.

C. Dispersion Relations

Recently, B. Pasquini *et al.*[11] developed a dispersion relation formalism that makes it possible to constrain the higher order terms (up to at least two pion threshold) in Eq. 4 from dispersion integrals over pion electro-production data. This extends the earlier work on Dispersion Relations for Real Compton Scattering.

The [non-Born] VCS amplitude can be expanded as:

$$\mathcal{T}^{\mu\nu}_{NB} = \sum_{i=1}^{12} F_i(\nu, Q^2, t)\rho_i^{\mu\nu}. \quad (8)$$

The $\rho_i^{\mu\nu}$ are 12 independent tensors in photon-polarization and nucleon spin-space. For example, $\rho_1^{\mu\nu} = q'^{\mu}q^{\nu} - q\cdot q' g^{\mu\nu}$. The amplitudes F_i are functions of the three invariants Q^2, t, and

$$\nu = \frac{s-u}{4M_p} = \frac{[q^0+q']_{\rm lab}}{2} - \frac{Q^2}{4M_p} \quad (9)$$

The $\rho_i^{\mu\nu}$ are defined such that the F_i are symmetric under photon crossing:

$$F_i(Q^2, -\nu, t) = F_i(Q^2, \nu, t). \quad (10)$$

The polarizabilities (Eq. 3) are linear combinations of $\overline{F}_i^{NB}(Q^2) = F_i(Q^2, \nu = 0, t = -Q^2)$. The linear q' dependence of the VCS amplitude $\mathcal{T}^{NB}$ [in the low energy limit] is contained in the tensors $\rho_i^{\mu\nu}$.

Assuming analyticity and an appropriate high energy behavior, the real and imaginary parts of each amplitude F_i will satisfy a Cauchy relation:

$$\Re\left[F_i^{NB}(Q^2,\nu,t)\right] \;=\; \int_{Th}^{\infty} \frac{\nu' d\nu'}{\nu'^2 - \nu^2} \Im\left[F_i(Q^2,\nu',t)\right] \tag{11}$$

By unitarity, $\Im[F_i]$ can be determined by a multipole decomposition of real and virtual photon absorption.

B. Pasquini *et al.*,[11] use a Regge theory analysis to show that the dispersion integrals of Eq. 11 converge for all F_i except F_1 and F_5. Furthermore, for $F_{3,4,6-12}$, they assert that the dispersion integrals are saturated by the $\gamma^* p \to N\pi$ amplitudes. For $F_{1,2,5}$, the dispersion integrals are evaluated up to $\nu_{\max} \approx 1.5$ GeV, and the asymptotic contribution is obtained formally by closing the contour in a semicircle of radius $\nu_{\max}$ in the complex-ν plane:

$$\Re\left[F_i^{NB}(Q^2,\nu,t)\right] \;=\; \Re\left[F_i^{\pi N}(Q^2,\nu,t)\right] + F_i^{\rm as}(Q^2,\nu,t) \tag{12}$$

$$\Re\left[F_i^{\pi N}(Q^2,\nu,t)\right] \;=\; \int_{-\nu_{\max}}^{\nu_{\max}} \frac{\nu' d\nu'}{\nu'^2 - \nu^2} \Im\left[F_i^{\pi N}(Q^2,\nu',t)\right] \tag{13}$$

For F_5, the [asymptotic] contribution from the complex contour at $\nu_{\max}$ is approximated by a ν-independent t-channel π^0 exchange:

$$F_5^{\rm as}(Q^2,\nu,t) \;=\; \frac{g_{\pi NN}}{M} \frac{F_{\pi^0\gamma\gamma}(Q^2)}{t - m_\pi^2} \tag{14}$$

This gives good agreement with the most recent experimental determination of the ($Q^2 = 0$) backward spin polarizability $\gamma_\pi = -\gamma_{E1} + \gamma_{M1} + \gamma_{E2} - \gamma_{M2}$ [2, 12].

The amplitude F_1 is approximated by the dispersion integral over the πN production amplitudes, plus a ν-independent t-channel exchange of an effective σ-meson:

$$F_1(Q^2,\nu,t) \;=\; F_1^{\pi N}(Q^2,\nu,t) + \left[\overline{F}_1(Q^2) - \overline{F}_1^{\pi N}(Q^2)\right] \frac{1 + Q^2/m_\sigma^2}{1 - t/m_\sigma^2} \tag{15}$$

$$\;=\; F_1^{\pi N}(Q^2,\nu,t) + \frac{\Delta\beta_M(Q^2)}{\alpha_{QED}} \sqrt{\frac{2\tilde{E}_p}{\tilde{E}_p + M}} \frac{1 + Q^2/m_\sigma^2}{1 - t/m_\sigma^2} \tag{16}$$

$$\Delta\beta_M(Q^2) \;=\; \left[\beta_M(Q^2) - \beta_M^{\pi N}(Q^2)\right] \tag{17}$$

$\beta_M^{\pi N}(Q^2)$ is the contribution to the magnetic polarizability obtained from the dispersion integral over the πN multipoles. The difference $\Delta\beta_M(Q^2)$ is a phenomenological function that must be fit to the RCS and VCS data as a function of Q^2.

Although the dispersion integral for F_2 converges in principle, in practice B. Pasquini *et al.,* find incomplete convergence from the πN multipoles. In particular, the $Q^2 \to 0$ limit of this dispersion integral over πN multipoles contributes 85% of the Baldin sum rule [13, 14]:

$$4M_p^2 \alpha_{QED} F_2(0,0,0) = \alpha_E + \beta_M = \frac{1}{2\pi^2} \int \sigma_\gamma(\nu') \frac{d\nu'}{\nu'^2} \quad (18)$$

$$= 13.69 \pm 0.14 \cdot 10^{-4}\,\mathrm{fm}^3 \quad (19)$$

$$4M_p^2 \alpha_{QED} F_2^{\pi N}(0,0,0) = 11.6 \cdot 10^{-4}\,\mathrm{fm}^3 \quad (20)$$

B. Pasquini *et al.,* approximate the contributions to F_2 beyond the πN multipoles with a ν- and t-independent function of Q^2

$$F_2^{\mathrm{NB}}(Q^2,\nu,t) = F_2^{\pi N}(Q^2,\nu,t) + \frac{\Delta\alpha_E(Q^2) + \Delta\beta_M(Q^2)}{4M_p^2 \alpha_{QED}} \sqrt{\frac{2\tilde{E}_p}{\tilde{E}_p + M}} \frac{\tilde{q}_0}{2M\mathbf{q}_{CM}^2}, \quad (21)$$

where $\Delta\alpha_E(Q^2) = \alpha_E(Q^2) - \alpha_E^{\pi N}(Q^2)$ is defined in the same way as $\Delta\beta_M$.

With the theoretical formalism and phenomenological ansätze outlined above, the dispersion relations are able to predict the full VCS amplitude through the Δ-resonance, in terms of just two phenomenological functions of Q^2: $\Delta\alpha_E$ and $\Delta\beta_M$. In particular, the dispersion relations are able to predict all of the spin polarizabilities, including their contributions to the observables of Eq. 3. The spin polarizability predictions are independent of the phenomenological terms $\Delta\alpha_E(Q^2)$ and $\Delta\beta_M(Q^2)$.

D. Previous Results

The existing data on the electric and magnetic polarizabilities are shown in Fig. 3. The scalar polarizabilities $\alpha(Q^2)$ and $\beta(Q^2)$ are extracted from the experimental observables by subtracting the vector polarizabilities calculated by the Dispersion Relations of B. Pasquini *et al.*[11]. The JLab E93-050 point at $Q^2 = 1$ GeV^2 was extracted both from two analysis: Low Energy Theorem, and Dispersion Relations. The Low Energy Theorem analysis used data spanning the full angular distribution below pion threshold. The Dispersion Relation analysis used data up to two pion threshold obtained with the proton spectrometer centered on $\theta_{\gamma\gamma} = 180^\circ$. The dispersion relation calculations in Fig. 3 are shown for a simple dipole approximation of the asymptotic contributions to the electric and magnetic polarizabilities:

$$\Delta\alpha_E(Q^2) = \frac{\Delta\alpha_E(0)}{\left[1 + Q^2/\Lambda_\alpha^2\right]^2} \quad (22)$$

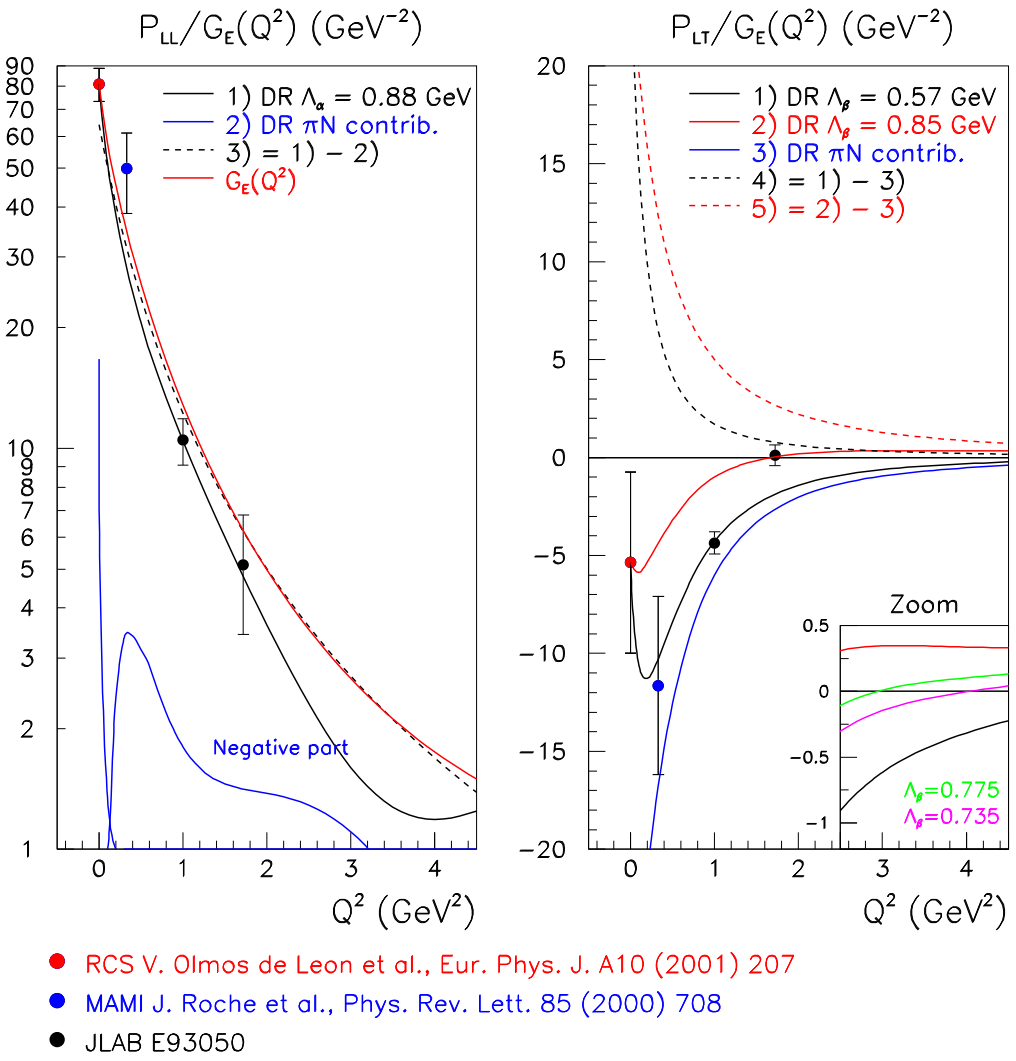

FIG. 3: Polarizability structure functions of the proton. P_{LL}/G_E is proportional to $\alpha_E(Q^2)$. P_{LT}/G_M is proportional to $-\beta_M(Q^2)$ plus spin polarizabilities. The real photon point is from Olmos de Leon, averaged with earlier RCS results. The Mainz $Q^2 = 0.33$ GeV^2 point is from J. Roche *et al.*[7]. The points at $Q^2 = 1.0$ and 1.7 GeV^2 are from Jefferson Lab E93-050. The E93-050 results are preliminary, the complete systematic errors are still under evaluation. The Bates VCS experiment [8] results will be at $Q^2 = 0.05$ GeV^2. The solid blue curves are the contributions of the πN dispersion relations, including the spin polarizabilities for P_{LT}. The dashed curves are the contributions of the terms $\Delta\alpha$ and $\Delta\beta$ of Eq. 22 & 23, with the parameters listed on the figure. The solid black lines are the complete DR calculations. These curves are fit to the $Q^2 = 0$ GeV^2 and $Q^2 = 1$ GeV^2 points. For P_{LL}, the solid red curve is proportional to $G_E(Q^2)$, normalized to the $Q^2 = 0$ point. For P_{LT}, the red and black curves are identical, except for different values of Λ_β. The zoom in the lower right corner of P_{LT} illustrates variation in P_{LT} for $\Lambda_\beta = 0.85$, 0.775, 0.735, and 0.57 GeV (top to bottom).

$$\Delta\beta_M(Q^2) \;=\; \frac{\Delta\beta_M(0)}{\left[1+Q^2/\Lambda_\beta^2\right]^2} \tag{23}$$

The value $\Lambda_\alpha = 0.88$ GeV is fit to the $Q^2 = 1$ GeV^2 point. The πN contribution $\alpha_E^{\pi N}(Q^2)$ changes sign at very low Q^2, and is everywhere much smaller than the experimental values for $\alpha_E(Q^2)$. Thus the high energy virtual excitations of the proton dominate the electric polarizability.

The electric polarizability closely follows the Electric form factor of the proton, $G_{E,p}(Q^2)$, as recently measured at Jefferson Lab [9, 10]. This implies that the electric polarization response is directly proportional to the charge density, at all distance scales.

The magnetic polarizability, when compared to the dispersion relation calculation illustrates a very strong cancellation of para- and dia-magnetism at all Q^2. The dispersion relation contribution $\beta^{\pi N}$ is strongly paramagnetic, whereas the asymptotic contribution $\Delta\beta_M$, whether fit to $Q^2 = 1$ or $Q^2 = 1.7$ GeV^2 is strongly diamagnetic.This destructive interference is also predicted at low Q^2 by Chiral Perturbation Theory [15]. In the Dispersion Relations, a large negative value for $\Delta\beta(Q^2)$ is a natural result, since this term results from a t-channel σ-meson exchange, which is parameterizes the (diamagnetic) contribution of the pion cloud.

II. EXPERIMENTAL PROPOSAL

We propose to use the 15 cm liquid H_2 target and the HRS pair in Hall A together with beam energies from 3.5 to 5.8 GeV to measure the $H(\vec{e}, e'p)\gamma$ cross section and beam helicity asymmetry at $Q^2 = 0.65$, 1.35, 3.0, and 4.0 GeV^2. At each Q^2 we will make measurements centered at threshold ($W = 1.073$ GeV) and at the $P_{33}(1232)$ resonance, which also corresponds very nearly to the two pion threshold. The angular settings at each Q^2, W pair are discussed below. At $Q^2 = 3$ and 4 GeV^2, the experiment takes advantage of the large Lorentz boost of the proton to cover a large acceptance (including out of plane) in a single setting of the HRS pair. We will take high statistics data in small bins in W and $\Theta_{\gamma\gamma}^{CM}$.

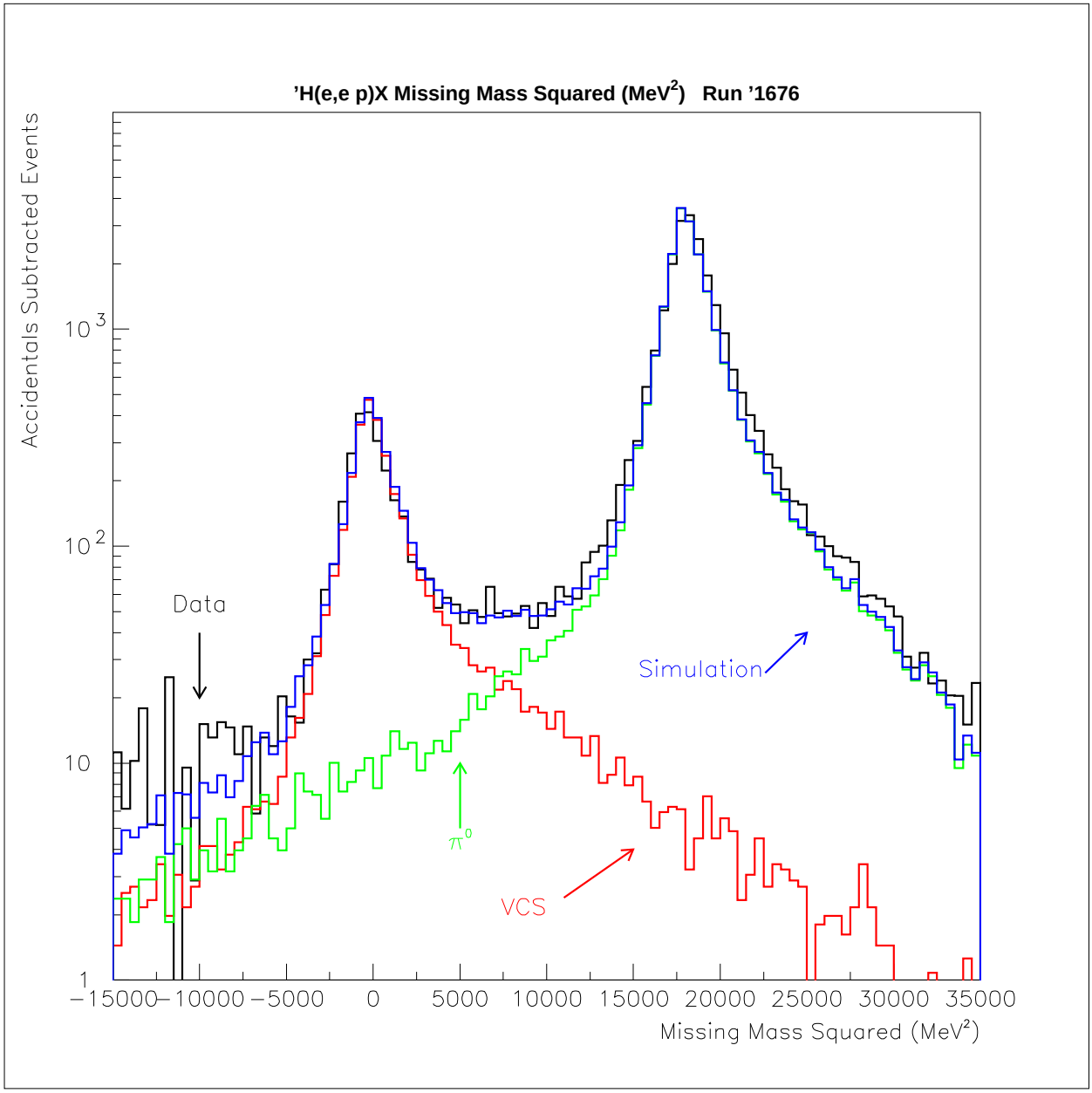

FIG. 4: Missing mass resolution for the $\mathrm{H}(e,e'p)X$ reaction, obtained in JLab E93-050 at $Q^2 = 1$ GeV^2. The $\mathrm{H}(e,e'p)\gamma$ and $\mathrm{H}(e,e'p)\pi^0$ processes are clearly separated, and the simulation accurately describes the line-shape.

A. Separation of $\mathbf{H}(e,e'p)\gamma$ and $\mathbf{H}(e,e'p)\pi^0$ Reactions

Fig. 4 displays sample missing mass spectra for the $\mathrm{H}(e,e'p)X$ reaction from JLab VCS experiment E93-050. Fig. 5 displays simulations for the present proposal at $Q^2 = 4$ GeV^2.

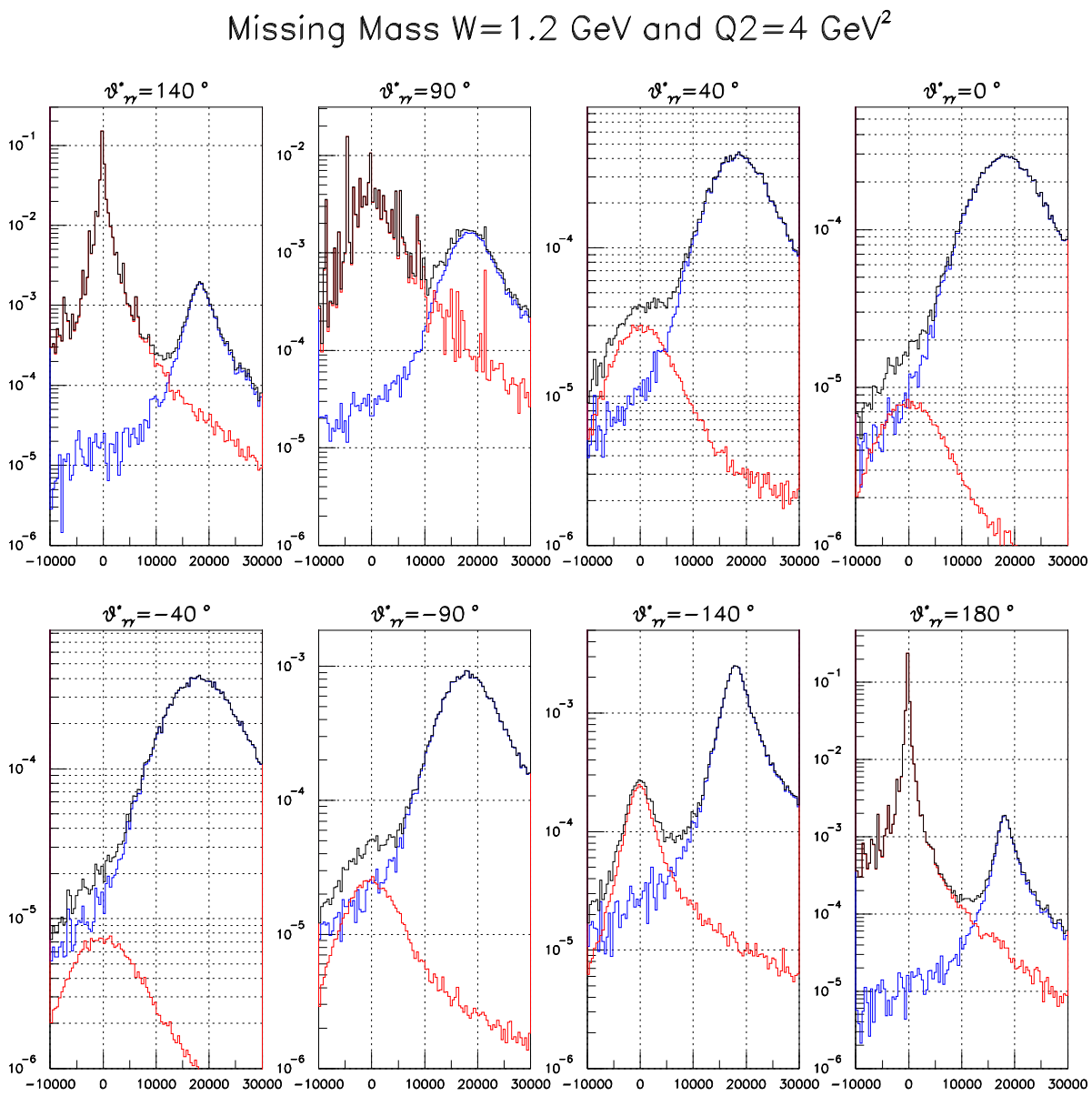

FIG. 5: Projected missing mass resolution for the H$(e,e'p)X$ reaction, at $Q^2 = 4$ GeV^2 and $W = 1.2$ GeV. $\theta_{\gamma\gamma}^{CM}$ is the angle between the $\vec{q}$ and missing particle directions, in the electron scattering plane. The incident beam and scattered electron directions lie at positive $\theta_{\gamma\gamma}^{CM}$. The strong kinematic dependence of the line-shape reflects the boost. The simulation includes all of the resolution effects from E93-050. Due to the increase in beam energy from 4 to 5.8 GeV, the final electron and proton momenta here are similar to the values in E93050. The VCS/π^0 separation is uniformly better at $W = 1.1$ GeV, since the VCS cross section is larger and the π^0 cross section is smaller. At $Q^2 = 3$ GeV^2, the M_X^2 spectra are qualitatively the same as at $Q^4 = 4$ GeV^2.

At $Q^2 = 3$ GeV^2 and 4 GeV^2, the H$(e,e'p)\gamma$ and H$(e,e'p)\pi^0$ processes are well separated by the HRS^2 resolution in the backward direction and in the vicinity of the Bethe-Heitler peaks. Separation for $-90^\circ < \theta_{\gamma\gamma}^{CM} < 40^\circ$ would require detection of the final photon in triple coincidence. Experiment E93-050 demonstrates that the VCS channel can be separated at $Q^2 = 0.65$, and 1.35 GeV^2.

B. Sensitivity to Generalized Polarizabilities

In Figs. 6 and 7 we show the dependence of the differential cross section on the generalized polarizabilities. In order to illustrate the angular distributions relative to the electron scattering plane we define the CM longitude and latitude angles $\Theta_{\gamma\gamma}^{CM}$ and $\Phi_{\gamma\gamma}$, respectively. The electron scattering plane defines $\Phi_{\gamma\gamma} = 0$ and the direction **q = k - k'** defines the prime meridian $\Theta_{\gamma\gamma}^{CM} = 0$. The sign convention for $\Theta_{\gamma\gamma}^{CM}$ is chosen such that the Bethe-Heitler peaks (in the direction of the incident and scattered electrons) lie at positive values of $\Theta_{\gamma\gamma}^{CM}$. Note that for $\Phi_{\gamma\gamma} = 0$, the polar angle $\theta_{\gamma\gamma}^{CM}$ and the longitude $\Theta_{\gamma\gamma}^{CM}$ coincide.

Figs. 8 and 9 zoom on the angular range $-180^\circ \leq \Theta_{\gamma^*\gamma} \leq -90^\circ$, for $Q^2 = 4.0$, and 3.0 GeV^2, respectively, at $W = 1.2$ GeV.

The angular distributions provide our sensitivity to the polarizabilities. Our proposed measurements in 20 MeV bins in W from 0.95 to 1.25 GeV will provide a test of the Dispersion Relation formalism. In particular, the W-dependence is a test of whether the DR adequately describe the contributions of virtual channels beyond πN.

C. Single Spin Asymmetry

The single spin asymmetry H$(\vec{e},e'p)\gamma$ is dominated by the imaginary part of the BH–VCS interference. Since the BH is purely real, this observable therefore gives us direct access to the imaginary part of the VCS amplitude. As discussed above, the optical theorem links $\Im[VCS]$ with the on-shell [real and virtual] photo-absorption amplitudes. Therefore this observable is largely insensitive to the polarizabilities. However, we wish to measure the single spin asymmetry (above pion threshold), precisely because it offers us a calibration of the πN multipoles input to the dispersion relation calculations.

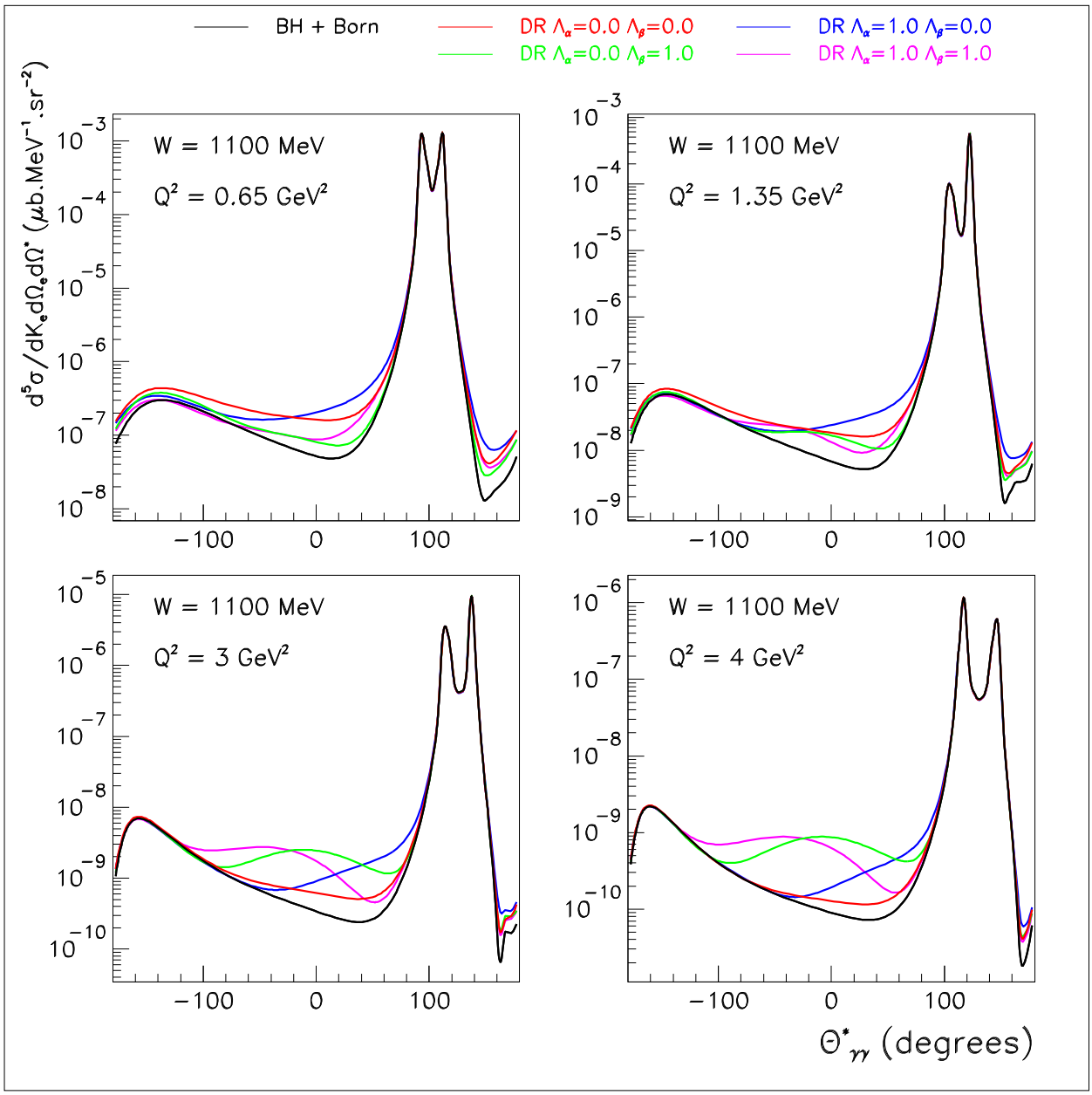

FIG. 6: Differential H$(e,e'p)\gamma$ cross sections $d^5\sigma/dk_e^{\rm lab}d\Omega_e^{\rm lab}d\Omega_{\gamma\gamma}^{CM}$ (mb/GeV/sr^2) at $W = 1.1$ GeV, for four values of Q^2. In each plot, the curves are: Bethe-Heitler+Born (black); Dispersion Relations (DR) with $(\Lambda_\alpha, \Lambda_\beta) = (1.0, 1.0)$ GeV (magenta); DR with $\Lambda_\alpha = 1.0$ GeV and $\Delta\beta(Q^2) = 0$ (blue); DR with $\Delta\alpha = 0$ and $\Lambda_\beta = 1$ GeV (green); and Dispersion Relations with $\Delta\alpha = 0 \Delta\beta = 0$ (red). The positive values of $\theta_{\gamma^*\gamma}$ correspond to $\phi_{\gamma^*\gamma} = 0$, whereas $\theta_{\gamma^*\gamma} < 0$ refers to $\phi_{\gamma^*\gamma} = 180$.

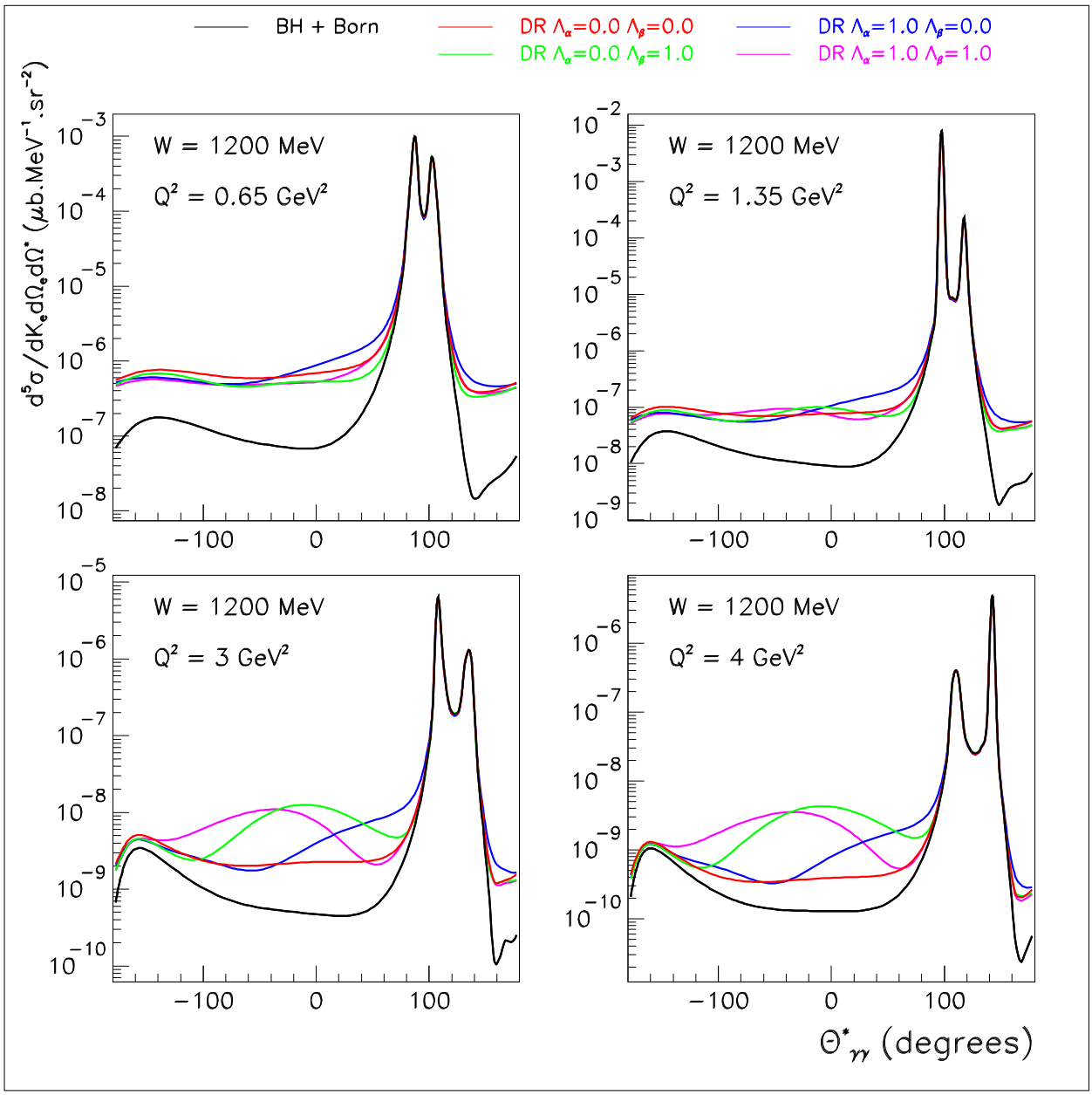

FIG. 7: Differential H$(e, e'p)\gamma$ cross sections at $W = 1.2$ GeV, for four values of Q^2, as a function of $\Theta^{CM}_{\gamma\gamma}$ (see text). The curves are defined in the same way as in Fig. 6.

D. Count Rates

Fig. 8 illustrates the coincidence acceptance for VCS at $Q^2 = 4.0$ GeV^2, $W = 1.2$ and the proton arm centered at $\Theta^{CM}_{\gamma\gamma} = -140$. Fig. 9 is the same figure, for $Q^2 = 3$ GeV^2. The simulations illustrate the large out-of-plane acceptance: roughly one third of the statistics

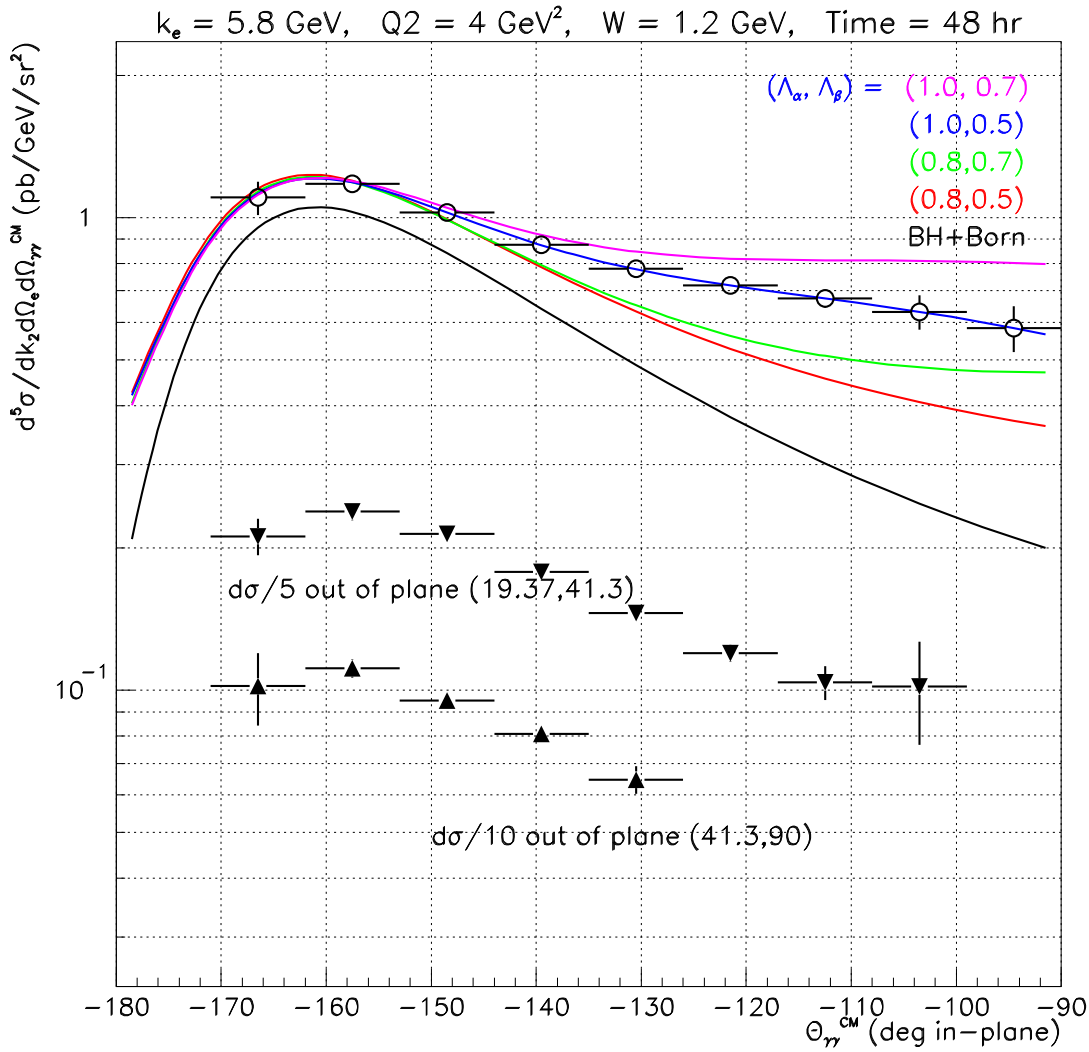

FIG. 8: Differential H$(e,e'p)\gamma$ cross sections as a function of $\Theta^{CM}_{\gamma^*\gamma}$. The other kinematic parameters are $k_e = 5.8$ GeV, $Q^2 = 4.0$ GeV^2, and $W = 1.2$ GeV. The curves are (from top to bottom) the Dispersion Relation predictions with the parameters $(\Lambda_\alpha, \Lambda_\beta) =$ (1.0, 0.7), (1.0, 0.5), (0.8, 0.7), (0.8, 0.5), in GeV. The black curve is the Bethe-Heitler + Born prediction. The error-bars superimposed on the $(\Lambda_\alpha, \Lambda_\beta) = (1.0,\ 0.5)$ curve represent the statistical precision after 48 hours of 80 μA on the 15 cm LH_2 target (50,000 fb^{-1}), with the proton spectrometer centered on $\Theta^{CM}_{\gamma\gamma} = -140°$. The statistical errors are shown in three bands in latitude: $(0, 19.4°)$; $(19.4°, 41.3°)$; $(41.3, 90°)$. These bands are chosen to equally subdivide the solid angle for each value of the the longitude variable $\Theta^{CM}_{\gamma^*\gamma}$. For clarity, the projected data in the out-of-plane bands are renormalized by 1/5 and 1/10. No theory curves are shown for the out of plane bins.

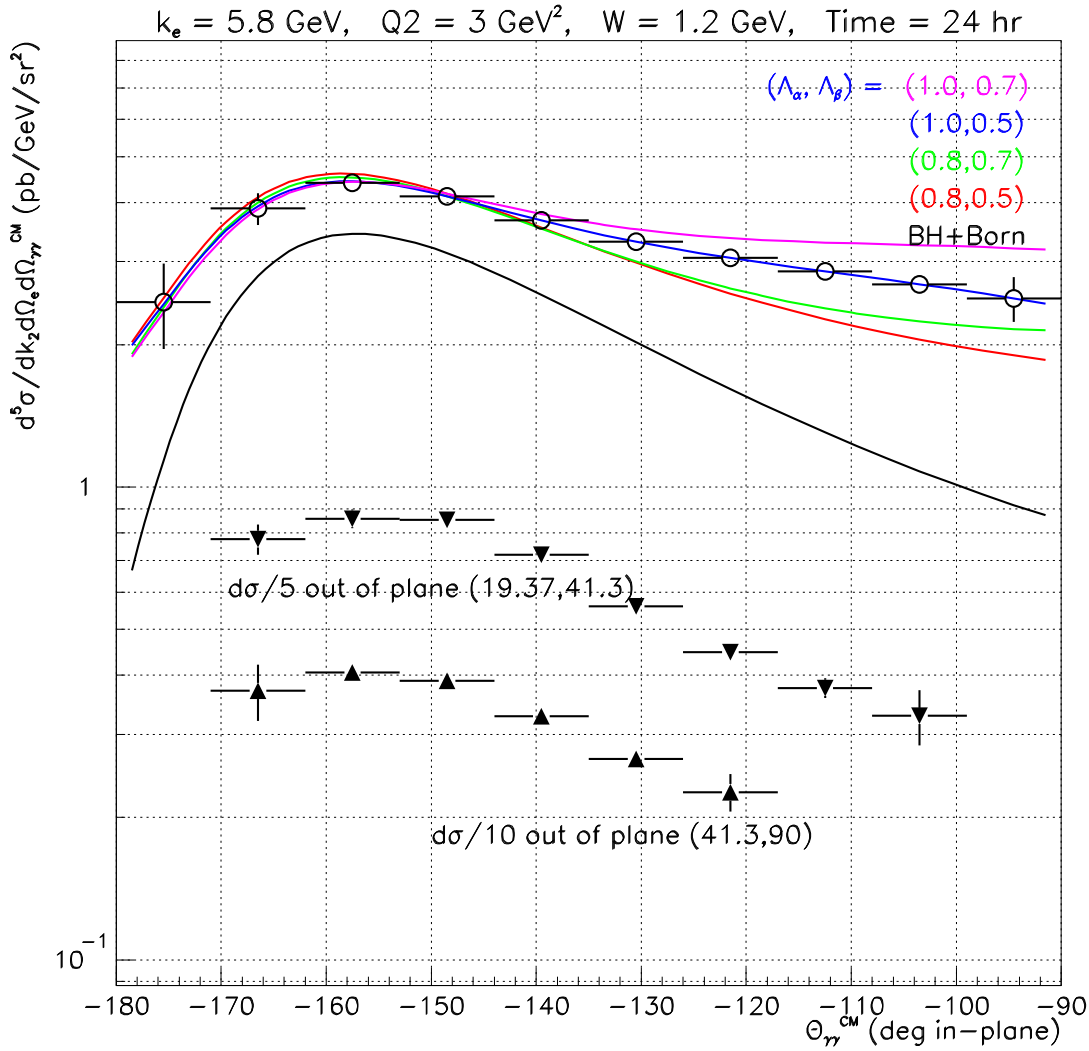

FIG. 9: Differential H$(e, e'p)\gamma$ cross sections as a function of $\Theta^{CM}_{\gamma^*\gamma}$. The other kinematic parameters are $k_e = 5.8$ GeV, $Q^2 = 3.0$ GeV^2, and $W = 1.2$ GeV. The statistics are obtained with 24 hours of 80 μA beam. The curves and simulated experimental results are obtained in the same way as for Fig. 8

.

lie at $|\Phi_{\gamma\gamma}| > 20°$. The simulations were done with just the Bethe-Heitler plus Born cross section. To obtain realistic count rate estimates, we scale the simulated cross section by the ratio of the DR and BH+B cross sections at the center of the acceptance (Figs. 6 & 7) The plots show a strong statistical sensitivity to the polarizabilities in the range $-140 < \Theta^{CM}_{\gamma^*\gamma} < -90°$. The variation of each of the polarizability parameters by ± 0.2 is chosen to

correspond to approximately the 2σ relative precision of the measurements in E93-050.

We will subdivide each acceptance into 9° degree bins in longitude, 3 bins of equal acceptance in latitude, and 20 MeV bins in W. We seek 7% statistics in the central bins of each setting. The precision of the W-dependence is illustrated in Fig. 10.

E. Calibrations

At $Q^2 = 3$ GeV^2 and 4 GeV^2, we will take coincidence $p(e,e'p)\gamma$ data at the Bethe-Heitler peaks, in order calibrate the absolute alignment of the spectrometer pair, and to normalize our results to the elastic form factors. We note that the angular changes in $\theta_{\gamma^*\gamma}$ at fixed Q^2, W for both production and calibration data does not require any changes to the electron arm, only the proton arm angle and momentum must be varied. We will use the ARC and/or EP apparatus to determine the beam energy. In E93-050, we found that our $H(e,e'p)X$ missing mass resolution is very sensitive to knowledge of the absolute beam energy.

F. Beam Time Request

Our request is

- 10 hours at $Q^2 = 0.66$ GeV^2.
- 14 hours at $Q^2 = 1.35$ GeV^2.
- 108 hours at $Q^2 = 4$ GeV^2,
- 60 hours at $Q^2 = 3$ GeV^2.
- Total request: 192 hours

Bibliography

[1] D. Babusci, G. Giordano, A. I. L'vov, G. Matone and A. M. Nathan, Phys. Rev. C **58**, 1013 (1998) [arXiv:hep-ph/9803347].

Q^2	W	ϵ	$\theta_{\gamma\gamma}$	$H(e,e'p)\gamma$ BH+B rate	$H(e,e'p)\gamma$ Full DR rate	Beam Time
(GeV^2)	(GeV)		(deg)	(hour^{-1})	(hour^{-1})	(hour)
$k = 5.8$ GeV						
4.0	1.0	0.82	-140	1000	1000	12
			-90	900	900	12
4.0	1.1	0.81	-140	700	800	34
			105=BH	$5.6 \cdot 10^4$	$5.6 \cdot 10^4$	2
4.0	1.2	0.79	-140	150	300	48
$k = 5.8$ GeV						
3.0	1.0	0.89	-140	$1.6 \cdot 10^4$	$1.6 \cdot 10^4$	4
			-90	2400	2400	12
3.0	1.1	0.88	-140	1800	1900	18
			BH	$6.1 \cdot 10^4$	$6.1 \cdot 10^4$	2
3.0	1.2	0.87	-140	620	1000	24
$k = 4.64$ GeV						
1.35	1.0	0.95	-135	$4 \cdot 10^4$	$4 \cdot 10^4$	1
			-90	$2 \cdot 10^4$	$2 \cdot 10^4$	1
1.35	1.1	0.94	-135	7200	8000	2
			-90	2400	2900	4
1.35	1.2	0.93	-135	2900	9000	2
			-90	1100	4400	4
$k = 3.50$ GeV						
0.65	1.0	0.96	-135	$8.8 \cdot 10^4$	$8.8 \cdot 10^4$	1
			-90	$4.8 \cdot 10^4$	$4.8 \cdot 10^4$	1
0.65	1.1	0.96	-135	$1.6 \cdot 10^4$	$1.8 \cdot 10^4$	2
			-90	6400	7000	2
0.65	1.2	0.95	-135	7200	$2 \cdot 10^4$	2
			-90	2400	$1 \cdot 10^4$	2

TABLE I: Hall A HRS[2] count rates and beam request for H$(e,e'p)\gamma$ reaction with 80 μA beam on 15 cm LH_2 target.

Q^2	W	$\theta_e^{\rm lab}$	$k'_{\rm lab}$	$\theta_{\mathbf{q}}$	$\Theta_{\gamma\gamma}^{CM}$	$\theta_p^{\rm lab}$	$p_p^{\rm lab}$
(GeV^2)	(GeV)	(deg)	(GeV)	(deg)	(deg)	(deg)	(GeV)
$k = 5.8$ GeV							
4.0	1.0	25.3	3.605	-31.2	-140	-30.5	2.936
					-90	-30.0	2.793
4.0	1.1	25.7	3.493	-29.7	-140	-27.9	2.998
					105=BH	-33.0	2.527
4.0	1.2	26.1	3.370	-28.2	-140	-25.3	3.041
3.0	1.0	20.4	4.138	-36.9	-140	-35.9	2.377
					-90	-35.3	2.258
3.0	1.1	20.6	4.026	-34.9	-140	-32.7	2.427
					105=BH	-39.0	2.051
3.0	1.2	21.0	3.903	-33.0	-140	-29.5	2.496
$k = 4.64$ GeV							
1.35	1.0	15.8	3.857	-48.5	-135	-46.8	1.391
					-90	-45.9	1.319
1.35	1.1	16.0	3.745	-44.8	-135	-40.6	1.447
					-90	-38.1	1.276
1.35	1.2	16.3	3.623	-41.1	-135	-34.9	1.522
					-90	-30.5	1.266
$k = 3.50$ GeV							
0.65	1.0	14.1	3.090	-56.2	-135	-53.6	0.908
					-90	-52.2	0.853
0.65	1.1	14.3	2.978	-50.2	-135	-44.0	0.976
					-90	-40.0	0.843
0.65	1.2	14.6	2.855	-44.4	-135	-35.5	1.062
					-90	-28.7	0.864

TABLE II: Hall A HRS^2 kinematics for H$(e, e'p)\gamma$ reaction

[2] V. Olmos de Leon *et al.*, Eur. Phys. J. A **10**, 207 (2001).

[3] P. A. Guichon, G. Q. Liu and A. W. Thomas, Nucl. Phys. A **591**, 606 (1995) [arXiv:nucl-th/9605031].

[4] A. Metz and D. Drechsel, Z. Phys. A **356**, 351 (1996).

[5] D. Drechsel, G. Knochlein, A. Metz and S. Scherer, Phys. Rev. C **55**, 424 (1997) [arXiv:nucl-th/9608061].

[6] P.A. Guichon, and M. Vanderhaeghen Prog. Part. Nucl. Phys. **41**, 125 (1998).

[7] J. Roche *et al.* [VCS Collaboration], Phys. Rev. Lett. **85**, 708 (2000) [arXiv:hep-ex/0007053].

[8] "Virtual Compton Scattering", Bates Linac Exp. 97-03, J. Shaw *et al.*.

[9] O. Gayou *et al.* Phys. Rev. Lett. **88**, 092301 (2002) [arXiv:nucl-ex/0111010].

[10] M. K. Jones *et al.* [Jefferson Lab Hall A Collaboration], Phys. Rev. Lett. **84**, 1398 (2000) [arXiv:nucl-ex/9910005].

[11] B. Pasquini, M. Gorchtein, D. Drechsel, A. Metz and M. Vanderhaeghen, Eur. Phys. J. A **11**, 185 (2001) [arXiv:hep-ph/0102335].

[12] A. I. L'vov and A. M. Nathan, Phys. Rev. C **59**, 1064 (1999) [arXiv:nucl-th/9807032].

[13] A.M. Baldin, *Nucl. Phys.*, **18**, 310 (1960),

[14] D. Babusci, G. Giordano and G. Matone, Phys. Rev. C **57**, 291 (1998) [arXiv:nucl-th/9710017].

[15] T. R. Hemmert, B. R. Holstein, G. Knochlein and D. Drechsel, Phys. Rev. D **62**, 014013 (2000) [arXiv:nucl-th/9910036].

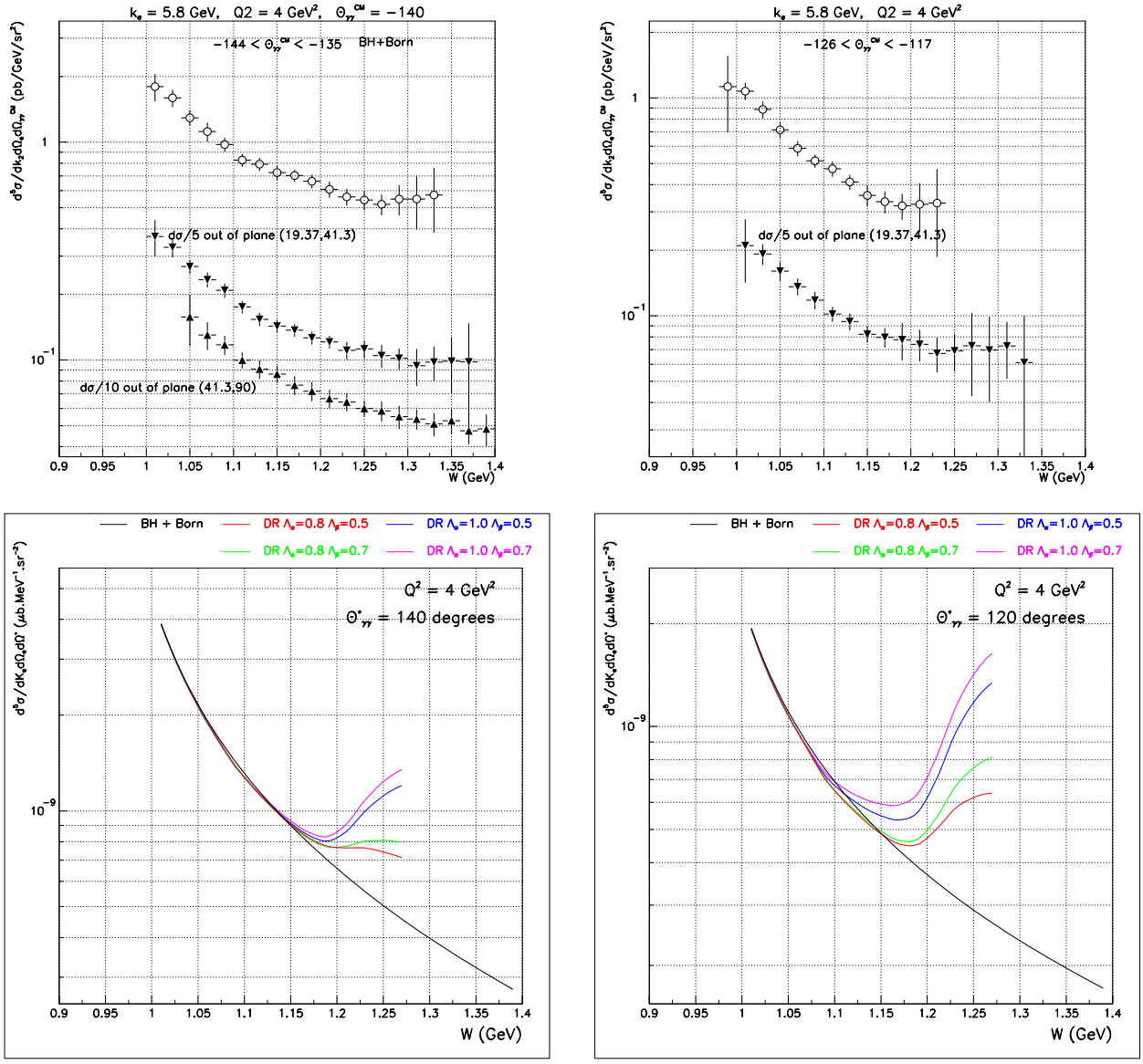

FIG. 10: Top figures: Combined anticipated statistics in 20 MeV bins in W (BH+Born cross section only) from settings W=1.1 GeV and W = 1.2 GeV, at Q^2 = 4.0 GeV^2 (W = 1.0 is not included in these statistics). The two plots are from bins $-146 \leq \Theta_{\gamma\gamma}^{CM} < -135°$ (left) and $-126 \leq \Theta_{\gamma\gamma}^{CM} < -117°$. The lattitude variable $\Phi_{\gamma\gamma}$ is divided into three bins: $(0, 19.4°)$, $(19.4°, 41.3°)$, and $(41.3°, 90°)$. At $\Theta_{\gamma\gamma}^{CM} \approx -120°$ only the first two bins in $\Phi_{\gamma\gamma}$ are populated by the acceptance. Bottom figures: Bethe-Heitler + Born (black) and Dispersion Relation curves at $\Theta_{\gamma\gamma}^{CM} = -140°$ (left) and $-120°$ (right). The theory curves are drawn in the electron scattering plane ($\Phi_{\gamma\gamma} = 0$).